DOI: 10.1002/srin.201100156 steel research int. 83 (2012) No. 1

Thermophysical Properties of a Fe-Cr-Mo Alloy in the Solid and Liquid Phase

R. K. Wunderlich[1)*], H. -J. Fecht[1)], I. Egry[2)], J. Etay[3)], L. Battezzati[4)], E. Ricci[5)], T. Matsushita[6)], and S. Seetharaman[6)]

[1)] Institute of Micro und Nanomaterials, Universität Ulm, Ulm, Germany
[2)] Institute of Materials Science in Space, German Aerospace Center Cologne, Germany
[3)] Centre National de la Recherche Scientifique CNRS-EPM, Grenoble, France
[4)] Università di Torino, Dipartimento di Chimica Inorganica, Chimica Fisica e Chimica dei Materiali, Università di Torino, Torino, Italy
[5)] CNR-IENI Genoa, Genoa, Italy
[6)] KTH, Department of Materials Science and Engineering, Division of Materials Process Science, Stockholm, Sweden
*Corresponding author; e-mail: rainer.wunderlich@uni-ulm.de

Results of a thermophysical characterization of a Fe-Cr-Mo alloy in the solid and liquid phases are reported. Methods applied include calorimetry, dilatometry; the laser flash technique for thermal diffusivity measurement and ultrasound pulse echo for the measurement of the room temperature sound velocities and elastic constants. Density in the liquid phase and surface tension were measured by optical dilatometry and by the oscillating drop method on electromagnetic levitated specimen. In addition, surface tension and viscosity were measured by the oscillating drop method on board parabolic flights under reduced gravity conditions. The methods applied and results obtained are presented. This work represents a collaborative effort, including round robin measurements in different laboratories for a characterization of the basic thermophysical properties needed for process simulation.

Submitted on 6 June 2011, accepted on 6 September 2011

Introduction

Thermophysical properties of Fe-based alloys in the high temperature solid and liquid phase are important input parameters in the modelling of a variety of industrial prodcution processes. Examples are casting and solidification [1, 2], strip casting of advanced steels [3, 4], melt flow control with magnetic fields [5] and welding [6]. The most basic properties needed for heat and fluid flow simulations include the specific heat capacity, enthalpy of fusion, fraction solid-liquid, thermal diffusivity, viscosity, density and the surface tension. The surface tension and its temperature coefficient are important parameters in welding simulations [7], in the simulation of bubble formation in the casting of steels and in strip casting [8, 9]. The measurement of these properties over any relevant temperature range is complicated by the difficulties of handling the liquid alloy over an extended period of time. Classical thermoanalytical methods in which the specimen is in contact with a container or support, such as DTA (differential thermal analysis), the oscillating cup for viscosity or the sessile drop method for surface tension measurements are susceptible to container reactions which can affect the outcome of thermophysical property measurements by contamination of the specimen or by the enthalpy associated with that reaction.

In order to improve this situation, containerless methods based on electromagnetic levitation can be applied [10]. The oscillating drop method [11] and optical dilatometry [12] have been applied successfully for the measurement of the surface tension and density in the liquid phase in ground-based electromagnetic levitation. The measurement of the viscosity by the oscillating drop method requires the absence of turbulence which is, however, present in electromagnetic levitation under normal gravity conditions due to the strong stirring forces of the levitation field. Under reduced gravity conditions, the levitation forces are much reduced resulting in laminar fluid flow which allows to apply the oscillating drop method to viscosity measurements [13, 14]. Inductive methods have been developed for non-contact calorimetry- and thermal relaxation time measurements in an electromagnetic levitation device under reduced gravity conditions [15].

In this contribution, results of a series of measurements of basic thermophysical properties affecting heat and fluid flow of an industrial Fe-alloy are described. In addition, calculations of the phase diagram were performed to which the experimental data are compared. The measurements were performed within the *ThermoLab* project [16], which is concerned with the measurement of the thermophysical properties of industrial alloys primarily in the liquid phase. *ThermoLab* is part of the European Space Agency's Micro Gravity Applications Support Programme (MAP). The Fe-Cr-Mo alloy was provided by an industrial partner of the project. In the following, an overview of the methods applied is given followed by the presentation and discussion of the results obtained. Round robin measurements in different laboratories can be applied to identify sources of systematic error and to improve calibration techniques.

Methods Applied

A multitude of thermoanalytical methods were applied including classical calorimetry, dilatometry and thermal diffusivity measurement by the laser flash method. Density in the liquid phase was measured by optical dilatometry in an electromagnetic levitation device. Surface tension and

viscosity were measured by the oscillating drop method in an electromagnetic levitation device on board a parabolic flight under reduced gravity conditions and in ground-based electromagnetic levitation.

Calorimetry. The specific heat capacity was measured in a high temperature DSC by the scanning method. The calorimeter (NETZSCH Jupiter DSC) consisted of a sample and reference pan connected by a heat flow plate both exposed, ideally, to the same heating power input by convection and radiation from the cylindrical heating oven. The measurement signal is derived from the temperature difference between the sample and reference container expressed in terms of a heat flow. First, a baseline run with empty sample containers, followed by a calibration run with an Al_2O_3 standard and a sample run are performed. Measurements in the solid phase are performed in a high density Al_2O_3 cup inserted in a Pt cup with a Pt lid. The Pt-lid is covered on the inside with a Y_2O_3 slurry to avoid possible alloying reactions of evaporated material with the Pt-metal at high temperature. For measurements in the liquid phase the Al_2O_3 inlay was coated with a Y_2O_3 slurry. The inlay was then dried in air for several hours and then heated to 1600 °C in argon. The sample runs were performed with cylindrical samples of nearly the same shape as the calibration sample.

In a second laboratory thermal analysis was performed with the high temperature differential scanning calorimeter of Setaram. The cell is made of alumina and the sample is contained in an alumina pan with some alumina powder to prevent it from sticking to the crucible walls. The sensor for the sample and reference cell is a thermopile and the instrumental output is a temperature difference. Therefore, the instrument is referred to as a differential thermal analyser (DTA). The cell is evacuated and purged several times before measuring under flowing Helium filtered to remove residual oxygen and water vapour. Various experiments were performed with heating rates $R_H = 2, 5, 10\,K\,min^{-1}$. The DTA cell was calibrated for the temperature and the heat flow by recording the melting temperature and heat of fusion of various pure metal samples (Al, Ag, Au, Cu, Ni) with $R_H = 2, 5,$ and $10\,K\,min^{-1}$. The frequency of sampling of the data points was one point every 1 to 3 s according to the heating or cooling rate for a total of 4800 point per file.

The specific heat capacity of the sample, C_p^S, is evaluated from the measured sample heat flow, W_S, the heat flow of the Al_2O_3 standard, W_{Ref}, and the baseline heat flow, W_{BL}, as:

$$C_p^S(T) = \frac{W_S(T) - W_{BL}(T)}{W_{Ref}(T) - W_{BL}(T)} \frac{m_S}{m_{Ref}} C_P^{Ref}(T) \qquad (1)$$

C_P^{Ref} refers to the specific heat capacity of the Al_2O_3 and m_S and m_{Ref} to the mass of the sample and the standard, respectively. The specific heat capacity thus obtained can be further refined with the specific heat capacity of an Fe or Ni standard measured after the sample run according to:

$$C_p^{SC}(T) = C_p^S(T) \frac{C_P^{Fe,S}(T)}{C_P^{Fe,m}(T)} \qquad (2)$$

with $C_P^{Fe,S}$ the literature value of the specific heat capacity of Fe, $C_P^{Fe,S}$ the measured heat capacity of Fe according to Eq. (1), and C_p^{SC} the final corrected specific heat capacity of the sample.

The enthalpy of a transformation with onset and end temperatures T_{ons} and T_{end}, respectively, is evaluated from the measured heat flow signal, W_S, according to:

$$\Delta H = S(T) \int_{Tons}^{Tend} dT\,[W_S(T) - B(T)] \qquad (3)$$

$B(T)$ corresponds to the extrapolated heat flow signal between T_{ons} and T_{end} which are supposed to lie in stable phase regions. In the two phase region $B(T)$ is proportional to the heat capacity of a changing fraction solid – liquid. The calorimeter sensitivity or response function $S(T)$ is obtained from a calibration run with an inert sample of known heat capacity similar to that applied for the specific heat measurement.

For the measurement of the enthalpy of fusion, additional calibrations with high-purity Ni and Fe were performed. From these measurements, correction factors, $f^{Ni}(T)$ and $f^{Fe}(T)$ to the calorimeter sensitivity function $S(T)$ were obtained. $f^{Ni}(T)$ and $f^{Fe}(T)$ express the effect of the sample shape change during melting with a resulting change in the heat flow conditions. Application of this correction presupposes that the sample to be investigated has the same wetting properties with the container material as Ni and Fe. The corrections amounted to $+8 \pm 2\%$ with respect to the ΔH_f values evaluated with the calorimeter sensitivity function $S(T)$ alone. As the melting temperature of pure Ni was within the solid-liquid range of the Fe of interest, the corrected enthalpy of fusion was obtained as:

$$\Delta H_S\,(true) = \Delta H_S\,(meas) \frac{\Delta H_{Ni}\,(true)}{\Delta H_{Ni}\,(meas)} \qquad (4)$$

with $\Delta H_S(meas)$ evaluated from Eq. (3). The evaluation of the enthalpy of fusion is demonstrated in **Figure 1** showing the melting transition of the Fe-Cr-Mo alloy and of a Ni

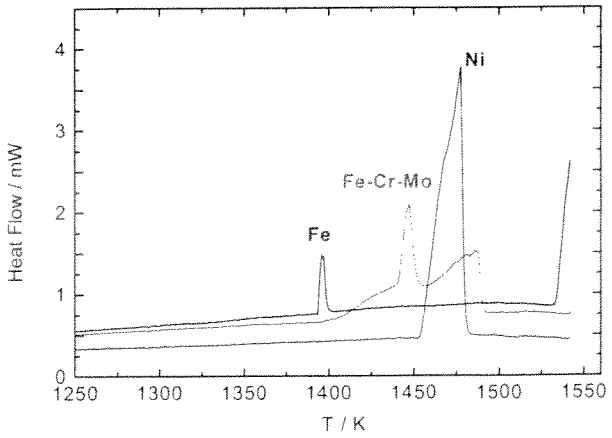

Figure 1. Melting transition of the Fe-Cr-Mo alloy and a Ni and aFe standard as indicated in figure. Heating rate $R_H = 10\,K\,min^{-1}$.

standard with onset temperature $T_m(Ni) = 1726.5 \pm 0.5$ K. In addition the heat flow from a Fe–standard with the δ-transition $T_\delta = 1666 \pm 0.5$ K and the onset of melting at $T_m(Fe) = 1805.9 \pm 0.5$ K is shown. Due to the overlap of the melting point of Ni with the melting range of the alloy, the enthalpy of fusion of Ni is ideal for the final calibration of the enthalpy of fusion of the alloy.

For the determination of the onset and end of melting, the finite thermal conductivity of the measurement set up needs to be considered. Thermal analysis instruments operating with a continuous heating rate exhibit a time lag between an enthalpy event in the sample and the indication of that event in the temperature sensing device resulting in a temperature shift between the true and the measured transformation temperatures. The size of the effect depends on the heating rate and sample mass. The onset and end of melting were obtained from heating-rate-dependent measurements and extrapolation to zero heating rate. The true liquidus temperature is identified with T_{end} for $R_H \rightarrow 0\,K\,min^{-1}$. For a sample mass of 25 ± 5 mg this correction amounted to $\Delta T = (-13.2 \pm 2)$ K with reference to a heating rate of $R_H = 20\,K\,min^{-1}$. For the onset of melting the similar effect evaluated from a Ni standard was obtained as $\Delta T = (-8 \pm 2)$ K.

Dilatometry. The dilatometer was a single pushrod type instrument with a maximum operating temperature of 1600 °C. The total length change of the sample and sample holder assembly is measured by induction. Calibration was performed by measuring an Al_2O_3 or a tungsten standard of similar dimension than the test sample. The calibration run was required to compensate for the thermal expansion of the instrument sample holder assembly. The sample measurement was followed by a further calibration run with a high-purity Fe sample. Measurements were performed under flowing argon with heating rates of $R_H = 5$ and $10\,K\,min^{-1}$. It was verified with the tungsten standard that the measured relative length change was not affected by the different heating rates.

Thermal diffusivity. Thermal diffusivity was measured by the laser flash method with a Shinku Riko laser flash apparatus (Model TC-7000H/MELT). The method is based on the analysis of the temperature response of a specimen of well-defined cylindrical geometry exposed to a short heating pulse by a laser. The details of the experimental methods are described elsewhere [17]. In order to orient the reader, only a brief description of the instruments used and the procedure adopted are presented. The parallelism of the disc shaped sample surfaces was ensured by measuring the sample thickness at a number of places. The experiments were carried out under purified argon atmosphere. By using a ZrO_2-CaO oxygen sensor, the oxygen partial pressure was found to be less than 10^{-18} atm. The sample was heated to 1532 K and cooled to room temperature at the rate of 6 K/min. The thermal diffusivity was measured during both heating and cooling cycles. At each temperature, the sample was kept for at least 20 min in order to ensure that the sample had attained thermal equilibrium. The measurements were carried out by repeating the laser shots at least five times. Thermal diffusivity was evaluated from the half time, $t_{1/2}$, required for the rear surface to reach half of the maximum temperature rise. Thermal diffusivity, λ, was calculated by Eq. (5), which is derived based on the analysis by Parker et al. [18]:

$$\lambda = K \frac{1.37 L^2}{\pi^2 t_{1/2}} \tag{5}$$

where L is the thickness of the sample. K, represents a correction factor which was introduced to correct for the influence of radiative heat loss [19, 20]. The coefficient K varies from 0 to 1 and attains a value of 1 under adiabatic conditions. $K = 0$ corresponds to the case of infinite heat loss with no temperature rise on the back of the specimen. The temperature response curve after having reached the maximum temperature was fitted by an exponential form, $\exp(-kt^*)$ where k is the coefficient of the temperature decrease and t^* is the dimensionless time normalized by $t_{1/2}$. The correction factor, K, was obtained as:

$$K = 1 - 2.790\,k + 9.862\,k^2 - 23.22\,k^3 + 20.21\,k^4 \tag{6}$$

by comparison with a standard of well known thermal diffusivity.

Density in the liquid phase. Density measurements in the liquid phase were performed by optical dilatometry in an electromagnetic levitation chamber [21]. The sample was processed in a protecting atmosphere of He in a levitation coil to which a current of 100 A and approximately 250 kHz is applied. The sample is positioned by forces due to interactions with the inhomogeneous magnetic field and melted by eddy currents that are induced within. Temperature control is achieved by a laminar flow of a He/Ar gas mixture. The temperature, T, is measured using an infrared pyrometer. For each sample, it is necessary to recalibrate the temperature with respect to the liquidus temperature, T_L. Values for T_L were obtained from the calorimetric measurements. If T_P is the output signal from the pyrometer, then the real temperature T is obtained using the following approximation derived from Wien's law:

$$\frac{1}{T} - \frac{1}{T_P} = \frac{1}{T_L} - \frac{1}{T_{L,P}} \tag{7}$$

In Eq. (7), $T_{L,P}$ is the pyrometer signal at liquidus temperature. Eq. (6) is valid only if the sample emissivity at the operating wavelength of the pyrometer $\varepsilon_\lambda(T)$ remains constant over the experimentally scanned range of temperature. This is a good approximation for most metals [22].

To measure the density based on the volume of the sample, shadowgraphs are taken from the levitated sample. The shadow image in a direction perpendicular to the levitation field axis is captured by means of a digital CCD camera and analyzed by an edge detection algorithm that locates the

edge curve, $R(\varphi)$, where R and φ are the radius and polar angle with respect to the drop centre. In order to eliminate the influence of oscillations, the edge curve is averaged over 1000 frames. It is then fitted by Legendre polynomials of order ≤ 6;

$$\langle R(\varphi)\rangle = \sum_{i=0}^{6} a_i P_i(\cos(\varphi)) \tag{8}$$

with P_i being the i-th Legendre polynomial. As can be shown by an analysis of top view images, the equilibrium shape of the sample is symmetric with respect to the vertical axis. Hence, its volume is calculated using the following integral:

$$V_P = \frac{2}{3}\pi \int_0^{\pi} < R(\varphi) >^3 \sin(\varphi) d\varphi \tag{9}$$

V_p is the volume in pixel units. It is related to the real volume V by a calibration procedure described in [21]. When M is the mass of the sample, the density, ρ, is calculated from $\rho = M/V$. The total error for the density is $\Delta\rho/\rho \leq 2\%$.

In order to check whether the mass of the sample remained constant over the duration of the experiment, each sample was weighed before and after the measurement. Only those measurements, where the sample had lost less than $\approx 0.1\%$ of its initial mass were accepted.

Surface tension and viscosity. Surface tension and viscosity were measured by the oscillating drop technique in an electromagnetic levitation device on board a parabolic flight and in ground based electromagnetic levitation. Details of the method and data evaluation have been described in detail elsewhere [12, 23, 24]. The specimen is suspended in a radio-frequency (rf) quadrupole field for positioning superimposed with a rf-dipole field for heating. The coil system and sample are contained in a high vacuum tight stainless steel processing vessel which can be operated with static or flowing gas as well as under high vacuum conditions. The temperature is measured by a two channel optical pyrometer operating in the wavelength ranges 1 – 2.5 μm and 3 – 4 μm. The specimen shape is recorded by two 200 Hz frame rate digital cameras directed along (axial) and perpendicular (radial) to the axis of the rf-dipole heating field.

Parabolic flights provide about 20 seconds of reduced gravity. This time is sufficient to heat, melt, heat into the liquid phase and cool a specimen to solidification. To assure complete solidification in one processing cycle convective cooling with an argon-helium gas mixture is applied. Specimen diameter was 6.5 mm corresponding to a sample mass of 0.82 g. A typical temperature-time diagram of processing in a single parabola is shown in **Figure 2**. During the cooling phase with the heater turned off and the positioning field reduced to minimum value, two pulses of the rf-heating field for the excitation of surface oscillations

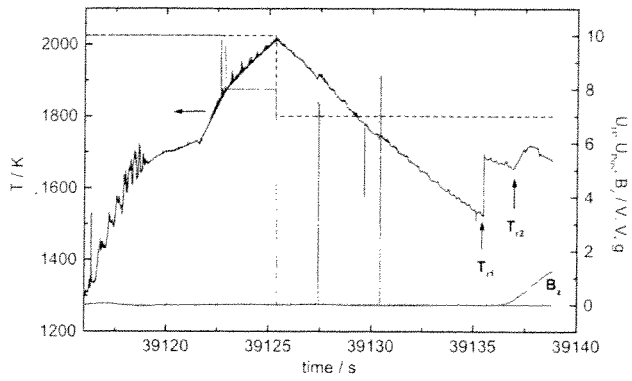

Figure 2. Temperature-time profile of processing an Fe alloy in the electromagnetic levitator on board a parabolic flight. The temperature is shown on the left hand ordinate, indicated by the horizontal arrow, the heater, red line, and positioner, dashed black line, control voltages and the residual acceleration, indicated by B_z, in units of the earth's gravitational constant, g, are shown on the right hand ordinate.

are applied. The specimens exhibited an undercooling of 160 K indicating that it was clean. Two recalescence events were observed indicated by temperatures T_{r1} and T_{r2} which apparently exhibited very different solidification velocities.

Under force-free conditions and in the absence of turbulence the surface tension, σ, and the viscosity, η, are given by:

$$\sigma = \frac{3}{8}\pi \nu^2 M \tag{10}$$

and

$$\eta = \frac{3}{20\pi}\frac{M}{R}\tau^{-1} \tag{11}$$

with M the sample mass, R the radius, ν the oscillation frequency and η the damping time constant of the surface oscillations.

Surface oscillations are extracted from the digital image recordings with a dedicated software [25]. Different measurements of sample shape deformation can be applied such as sum and difference of two perpendicular radii, the total projected area and the area difference with regard to a projected sphere of the same equilibrium radius. The analysis coordinate system can be rotated by a fixed angle or with a constant angular velocity. The surface oscillation frequency is obtained from a Fourier transform of typically 0.64 to 1.28 s time slices of the surface oscillation signal to an accuracy better 2%. For the evaluation of the surface tension according to Eq. (10) a small, - 1.5%, correction was applied to the measured oscillation frequency to account for the magnetic field pressure of the positioning field [26]. The correction is derived from the translational oscillations of the whole droplet with frequencies of $\nu_{trx} = 1.2$ and $\nu_{try} = 2.4$ Hz in the x and y directions, respectively [22, 27]. The damping time constant is derived either from an exponential envelope fit to the decaying surface oscillations

or from a linear fit to the logarithm of the absolute value of that signal. The evaluation of the damping time constant is often made difficult by a modulation of the oscillation signal coming from sample rotation and precession [28]. This increases the uncertainty of the viscosity determination to about ±30% [26].

Test specimens for the parabolic flight experiments with 6.5 mm diameter were milled from as-delivered material. The spheres were then ground and polished under water and ethanol for a shining surface finish, and subsequently they were annealed for 4 hr at 140 °C under high-vacuum conditions. The oxygen concentration of such prepared specimen was determined as < 60 ppm by the LECO hot gas extraction technique.

Ultrasound measurements. The sound velocities for longitudinal and transversal polarization, v_l and v_t, respectively, were measured by the ultrasound pulse echo technique. The set-up consisted of an ultrasonic pulse generator, a piezoelectric transducer and an oscilloscope for the measurement of the pulse run times. The device was operating at frequencies of 2.25 and 10 MHz. Velocities were measured on specimen of 1.39, 2.10 and 3.06 mm thickness with a diameter of 8.90 mm. Typical pulse echo times were between 0.5 and 2 μs. The accuracy of the pulse run time measurement was better 2%. The room temperature density was evaluated with the Archimedian method using two precisely machined rods with 5.0 mm diameter and 20 mm length giving a density of (7.854 ± 0.012) g cm^{-3}. From the measured sound velocities and the density, ρ, Poisson's ratio, μ, shear modulus, G, Young's modulus, E, and the bulk modulus, B, are obtained according to:

$$\mu = \frac{0.5 - (v_t/v_l)^2}{1 - (v_t/v_l)^2} \tag{12}$$

$$G = \rho v_t^2, \quad E = 2(1+\mu)G, \quad B = \frac{E}{3(1-2\mu)} \tag{13a,b,c}$$

Results and Discussion

Composition and microstructure. In **Figure 3**, a SEM back-scattered electron micrograph of the as-delivered alloy is shown. The microstructure is characterized by equiaxed grains with an average size of about 0.4 μm with a fine dispersion of precipitates. The bright precipitates with dimensions between 150 and 300 nm are rich in Mo, V and C and are presumably (Mo,V) carbides. Due to their smallness, the exact composition could not be determined by EDX. The identification of the precipitates with Mo–V carbides is also supported by the phase diagram calculations. In addition, a distinct Cr-rich- Fe-poor phase, indicated by the arrow in Figure 3, was present. The average composition of the as-delivered material obtained from EDX is given in **Table 1**.

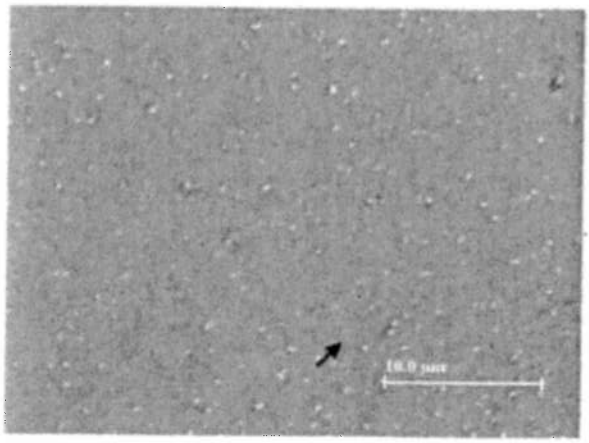

Figure 3. SEM micrograph of the microstructure of an as-delivered Fe-Cr-Mo alloy.

Carbon and oxygen were disregarded because of the difficulty of proper quantification of these elements by EDX. S could not be detected at a level > 100 ppm. The specimens processed on the parabolic flight solidified with a cooling rate of 35 Ks^{-1} to a temperature of 800 °C. The Si concentration was reduced from an average of 0.5 at% of the as-delivered specimen to an average of 0.35 at%. MoC precipitates of similar dimension as in the as delivered specimen were observed, however, at a reduced volume density. An SEM back-scattered electrons micrograph is shown in **Figure 4**.

Calorimetry and phase diagram calculations. In **Figure 5**, two thermograms of heating a specimen with R_H = and 15 and 20 K/min are shown. The thermograms were obtained from measurements of the specific heat capacity with baseline, sapphire calibration, and sample run. The agreement of the cp values obtained in the two measurements is better than 2%. Thermograms obtained in the second heating of specimens melted and solidified with $R_{H,C} = 20\,\mathrm{K\,min^{-1}}$ show the same thermal features. In **Figure 6**, the melting transition and solidification are shown in more detail. The specific heat measurements were performed with sample masses of (120 ± 20) mg while measurements of the enthalpy of fusion and of the onset and end of melting were performed with sample masses of (25 ± 5) mg. The large sample mass used for the specific heat capacity measurement is the reason why details of the melting transition are not well resolved in the latter.

On cooling the specimen consistently exhibited an undercooling of the onset of solidification by 60 – 90 K.

Table 1. Composition of investigated Fe-alloy in atomic%.

Element	Si	V	Cr	Mn	Mo	Fe
Concentration at%	0.5 ± 0.1	0.6 ± 0.1	6.0 ± 0.5	0.6 ± 0.5	1.3 ± 0.2	91.0 ± 0.5

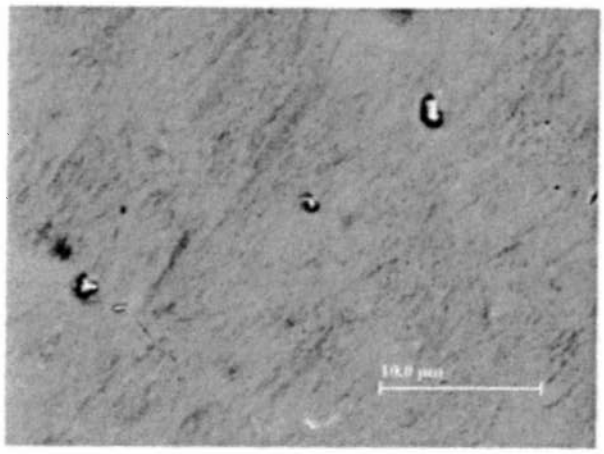

Figure 4. SEM micrograph of the microstructureof a Fe-Cr-Mo alloy solidified in the parabolic flight experiment.

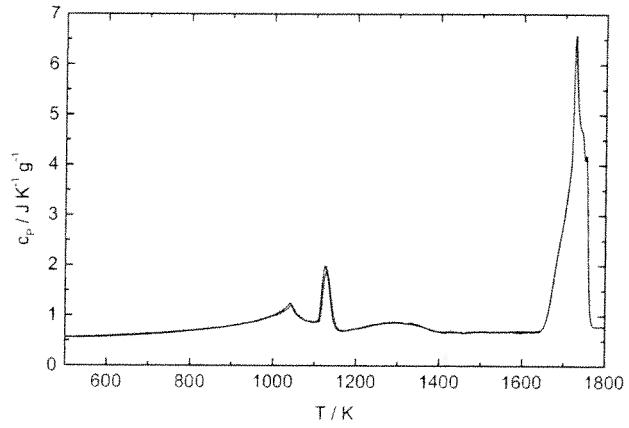

Figure 5. Specific heat capacity of Fe-Cr-Mo alloy in the solid and liquid phase.HTDSC. Superposition of two experiment runs with R_H = 15 and 20 K min^{-1}, red and blue line respectively.

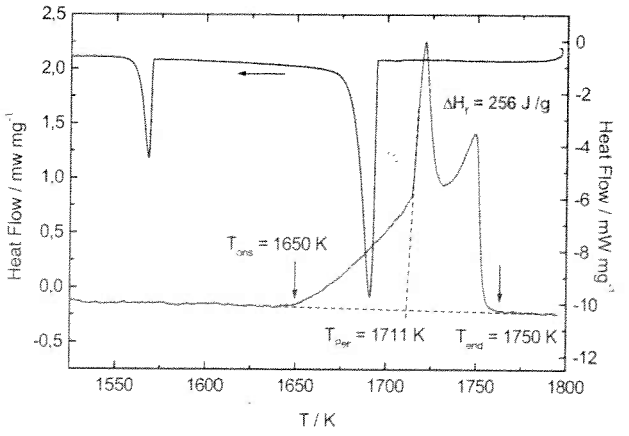

Figure 6. Melting transition, and solidification, indicated by leftward arrow, of Fe-Cr-Mo alloy. Heat flows are shown on the left and right hand ordinate for heating and cooling, respectively. HTDSC, $R_{H,C}$ = 20 K min^{-1}.

As such, the solidus and liquidus temperatures could only be evaluated from heating runs. The thermal profile obtained on cooling in the HTDSC bears some resemblance to the temperature-time profile obtained on the parabolic flight shown in Figure 2. In the microgravity experiment, a second temperature rise near the end of the microgravity period is apparent that is consistent with behaviour expected for an alloy exhibiting a transformation from metastable to the stable phase. This type of behaviour is commonly seen in Fe-Cr-Ni alloy steels and is known as double recalescence [29, 30]. The first recalescence event is presumably associated with the formation of the ferritic δ –phase, the second with the peritectic formation of the austenitic phase. The two nucleation events appearing in the HTDSC cooling curve shown in **Figure 7** were observed reproducibly. A large variation in the onset temperature of the second exothermal solidification event with respect to that of the first between 40 and 200 K was observed. With respect to the liquidus temperature the first nucleation event on cooling exhibited an undercooling between 40 and 80 K. Such behaviour is typical for peritectic solidification systems [31] although the undercoolings reported here are larger than those observed for similar cooling rates in steels. On further cooling with $R_C = 20\,\mathrm{K\,min^{-1}}$, no calorimetric signal for the formation of the (Mo,V) – carbides is apparent.

The onset and end temperatures of melting were obtained from heating-rate dependent measurements and extrapolation to zero heating rate. In addition a correction with regard to the onset of melting of a Ni standard of the same mass was applied. The following temperatures for the onset of melting and the liquidus temperature were obtained:

$$T_{ons} = (1658 \pm 6.0)\,\mathrm{K}$$

$$T_{liq} = (1757 \pm 6.0)\,\mathrm{K}$$

The uncertainty reflects the reproducibility of the temperatures. Comparison between the onset temperature of melting, the temperature of maximum heat flow of the peritectic transition and the end of melting with the calculated phase diagram qualifies the present alloy as hyper peritectic with a carbon content of about 0.5 mass % C.

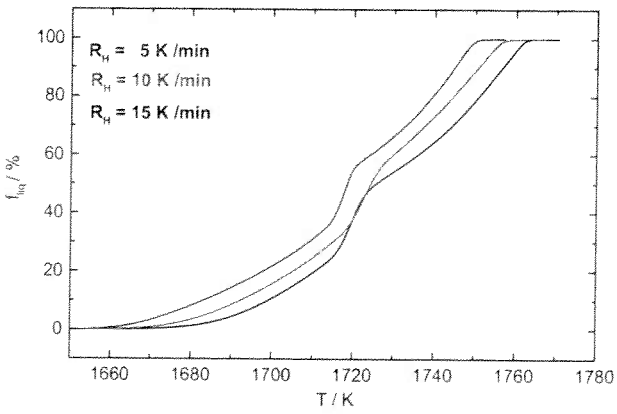

Figure 7. Fraction liquid on heating for heating rates R_H = 5, 10 and 15 K/min from top to bottom, respectively.

The enthalpy of fusion, ΔH_f, was evaluated in two laboratories from measurements with heating rates $R_H = 5$, 15 and 20 K/min. Calibration was performed with Ni as described in section 2.3. Correction factors in different measurements series using different sample holders and cups ranged from 0.97 to 1.10. Results are summarized in **Table 2** showing the average values of ΔH_f obtained in a series of experiments in the participating laboratories. This value is very close to that of pure Fe with $\Delta H_f(\mathrm{Fe}) = 247\ \mathrm{J\,g^{-1}}$ as to be expected.

The fraction solid/liquid on heating was obtained from the heat flow curve during melting as shown in Figure 6 under the assumption of a constant enthalpy of fusion as a function of temperature-composition. In **Figure 7**, the fraction liquid on heating as a function of temperature for heating rates $R_H = 5$, 10 and 15 K/min. Because of the undercooling on cooling the fraction solid on cooling is not shown.

The specific heat capacity was measured in a series of experiments with heating rates of $R_H = 15$ and 20 K min^{-1}. An endothermal reaction is observed in the temperature range between 700 and 1200 °C. As such, the values of the specific heat capacity in this temperature range do not correspond to a thermal equilibrium situation. Under these conditions, measured specific heat values will depend on the heating rate. Values of the specific heat capacity are listed in **Table 3**. Ni and Fe exhibited the same wetting with the sample container resulting in the same sample shape in the liquid phase. The contact angle measured through the liquid was 130 –140° for all three substances. Thus, in addition to the Al_2O_3 standard used in the standard specific heat measurements additional runs with Ni and Fe specimen in the liquid phase were performed to obtain a correction factor for the evaluation of specific heat capacity value of the Fe-Cr-Mo sample in the liquid phase. The much larger uncertainty of the specific heat capacity in the liquid phase stems from the above-mentioned difficulty of measuring in the liquid phase. In the present case this is mainly associated with the change in the heat flow conditions upon melting. In the liquid phase at $T_{liq} + 20$ K, the Neumann-Koop ideal mixing rule would result in a specific heat capacity of $c_P(T_{liq} + 20\ \mathrm{K}) = 0.80\ \mathrm{J\,K^{-1}\,g^{-1}}$ close to the experimental result.

The total enthalpy change between $T = 293$ and 1803 K is obtained from integration of the specific heat capacity as a function of temperature as:

$$\Delta H\,(293 \rightarrow 1803)\,\mathrm{K} = (1403 \pm 12)\,\mathrm{J/g}.$$

A constant heat capacity of 0.55 J K^{-1} g^{-1} was assumed in the temperature range between 293 and 473 K. In **Figure 8**, enthalpy as a function of temperature with reference to $H(293\ \mathrm{K}) = 0\ \mathrm{J\,g^{-1}}$ is shown.

In **Figure 9**, the calculated phase diagram of a Fe-5.3at%Cr-2.13at%Mo-0.53at%V-0.56at%Mn-0.24at%Si is shown as a function of the C content. The phase diagram was calculated with the *ThermoCalc* software package using theTCFE3 database for Fe alloys. From the measured solidus and liquidus temperatures the alloy can be considered to be slightly hyperperitectic. Following the calculated phase diagram the characteristic thermal events observed on heating are listed in **Table 4**.

Thermal expansion. The relative length change of the Fe-Cr-Mo alloy on heating and cooling is shown in **Figure 10**. L_o is the sample length measured at RT and dL refers to the total length change from the starting temperature of the measurement at 40 °C. Measurements were performed with a heating and cooling rate of $R_{H,C} = 10$ K/min. Maximum temperature was 1350 °C. On heating, the decrease of dL /L_o at $T = 1035$ K is caused by the onset of the ferromagnetic transition. Further shrinkage is caused by the austenitic γ transition. On cooling, besides an undercooling of the of the γ transition of about 200 K the relative length change is very well reproducible on heating and cooling. In **Figure 12**, the coefficient of linear thermal

Table 2. Enthalpies of fusion in J g^{-1} obtained in different laboratories with different thermoanalytical equipment.

Lab A	Lab B
250 ± 6	246 ± 10

Table 3. Specific heat capacity of Fe-Cr-Mo alloy in the solid and liquid phase. Average of three measurements.

T/K	C_P/J K^{-1} g^{-1}	T/K	C_P/J K^{-1} g^{-1}
473	0.55 ± 0.02	1173	0.70 ± 0.02
573	0.58 ± 0.02	1273	0.85 ± 0.02
673	0.62 ± 0.02	1373	0.73 ± 0.02
773	0.67 ± 0.02	1473	0.68 ± 0.02
873	0.75 ± 0.02	1573	0.69 ± 0.02
973	0.91 ± 0.02	1803 liq	0.78 ± 0.14
1073	0.90 ± 0.02		

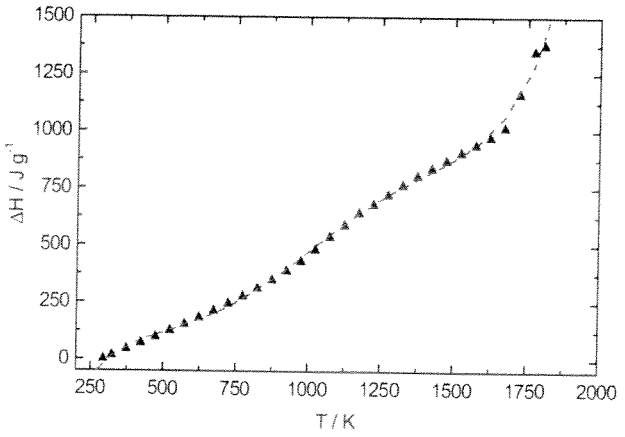

Figure 8. Enthalpy of Fe-Cr-Mn alloy as a function of temperature with H(293 K) set to zero. The dashed line represents a fifth order polynomial fit.

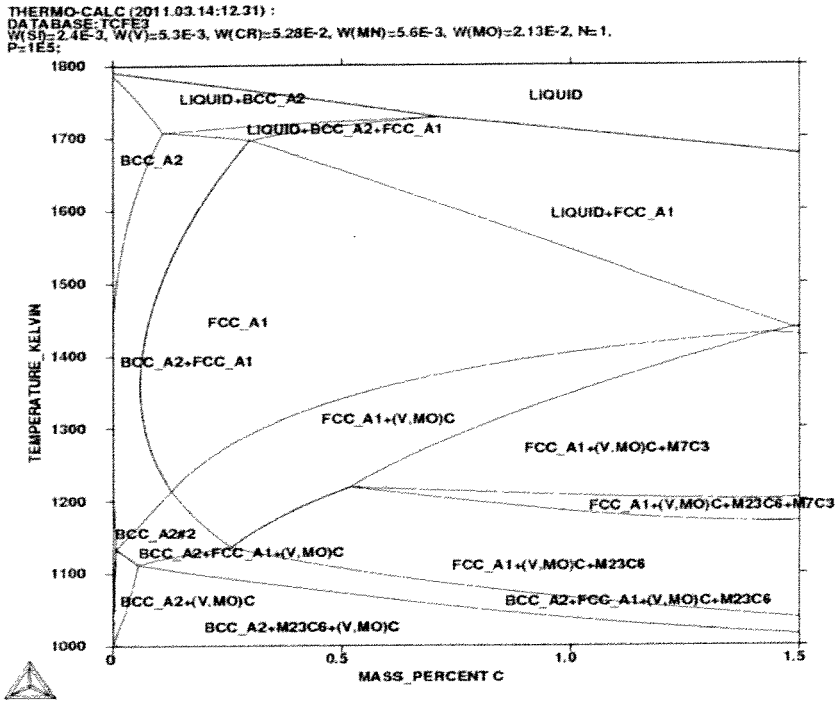

Figure 9. Calculated phase diagram of the Fe-Cr-Mo alloy as a function of C content. Calculation performed with the ThermoCalc software.

expansion of the Fe-Cr-Mo alloy in comparison with that of a high-purity Fe standard and the relative length change, dL/L_o, of the Fe standard are shown. The γ and δ phase transitions of the Fe standard are clearly exhibited at $T_\gamma = 1203$ K and $T_\delta = 1676$ K, respectively, as compared to tabulated values of $T_\gamma = 1185$ K and $T_\delta = 1667$ K. This large temperature difference is originates from the temperature difference between the measurement position and sample. The shrinkage at the γ phase transition of the Fe standard is obtained as $-7.25\ 10^{-3}$. The corresponding value for the Fe-Cr-Mo alloy in the temperature range between 1031 K and 1165 K is $-7.39\ 10^{-4}$. The magnetic and the γ-phase transition are more clearly exhibited in the temperature dependence of the coefficient of linear thermal expansion shown in **Figure 11** together with that of an Fe-standard. The coefficient of linear thermal expansion obtained in this work is very well within the range of values listed for Cr-Mo steels.

Table 4. Thermal events on heating with $R_H = 15$ K/min.

$T_{max} = 1038$ K	ferromagnetic transition
$T_{max} = 1121$ K	austenite formation
$T_{ons} = 1163$ K, $T_{max} = (1288 \pm 10)$ K, $T_{end} = (1423 \pm 15)$ K	dissolution of (Mo,V) carbides
$T_{ons} = (1667 \pm 5)$ K, $T_{end} = (1772 \pm 4)$ K	melting
$T_{max1} = (1711 \pm 6)$ K	onset of the peritectic transition

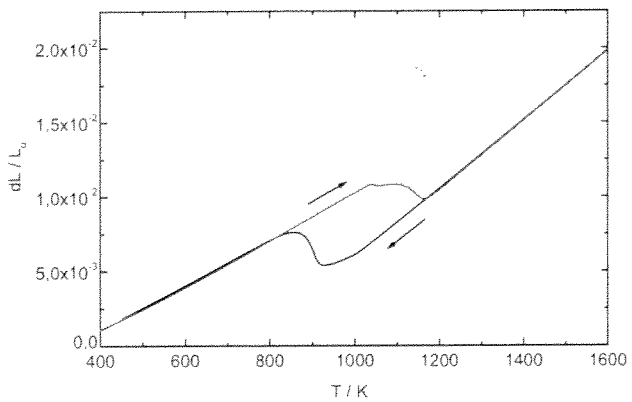

Figure 10. Relative length change of Fe-Cr-Mo alloy. Heating (up arrow) and cooling (down arrow) with $R_{H,C} = 10$ K min^{-1}.

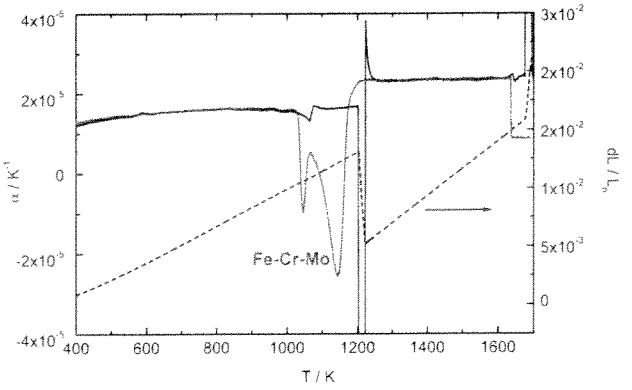

Figure 11. Coefficient of linear thermal expansion, α, as a function of temperature of the Fe-Cr-Mo alloy, red curve, and of a Fe standard, blue curve, shown on the left hand ordinate. dL/L_o of the Fe standard, indicated by the arrow, is shown on the right hand ordinate.

Thermal diffusivity. Thermal diffusivity as a function of temperature obtained with the laser flash method is shown in **Figure 12**. The minimum of thermal diffusivity is observed at the ferromagnetic transition at T = 1030 K. From the measured specific heat capacity, density at room temperature and coefficient of linear thermal expansion the thermal conductivity, κ, can be calculated according to $\kappa(T) = \lambda(T)\,\rho(T)\,c_P(T)$ with $\lambda(T)$ and $\rho(T)$ the thermal diffusivity and density, respectively. The density in the solid phase was obtained from measurement of the density at RT by the Archimedian method as $\rho(RT) = 7.85\ g/cm^3$ and the measured coefficient of linear thermal expansion. The specific heat capacity was taken from the measurement shown in **Figure 5**. Results are shown in **Figure 13**. It must be considered, however, that in the temperature range between 1163 and 1420 K the measured specific heat capacity does not correspond to a thermodynamic equilibrium value. It is increased because of the dissolution of the carbides in this temperature range. Extrapolation of the specific heat capacity values in the temperature range between 1400 and 1500 K back to the austenite phase transition would result in a reduction of the thermal conductivity at T = 1250 K by about 20% as compared to the value shown in Figure 12. Values of the thermal conductivity in this temperature range obtained by measurements of the thermal diffusivity and specific heat capacity may be different from values obtained by direct measurement with the heat flux method. The values obtained for the thermal conductivity in the temperature range between 473 and 873 K are about a factor of two higher than those of the high-alloyed 304 L steel. The thermal conductivity of pure Fe is 44 $WK^{-1}\,m^{-1}$ at 693 K.

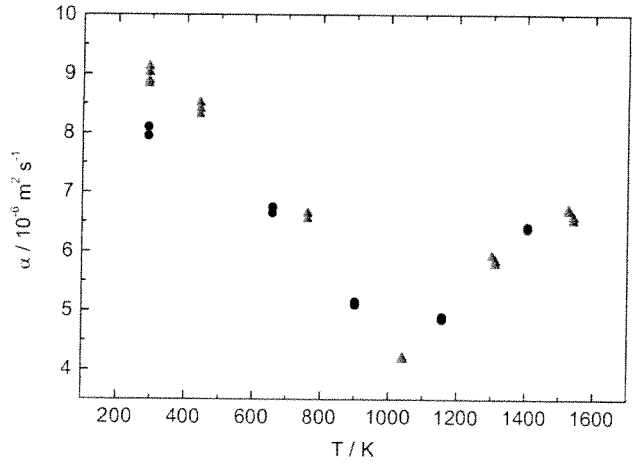

Figure 12. Thermal diffusivity on heating and cooling of Fe-Cr-Mo alloy. ● heating, ▲ cooling.

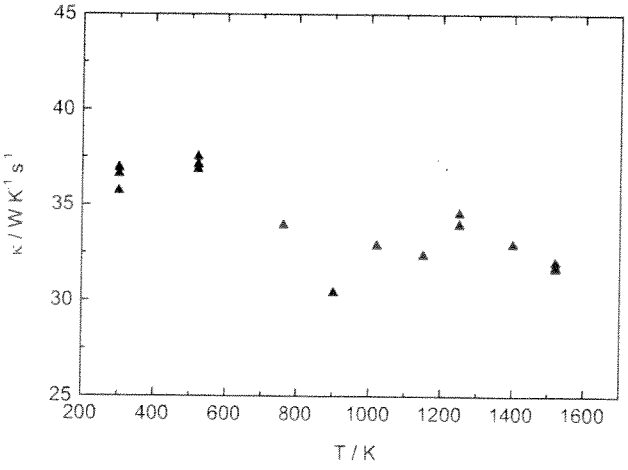

Figure 13. Thermal conductivity of Fe-Cr-Mo alloy. Calculated from measuredthermal diffusivity, heat capacity and density. Data for heating and cooling.

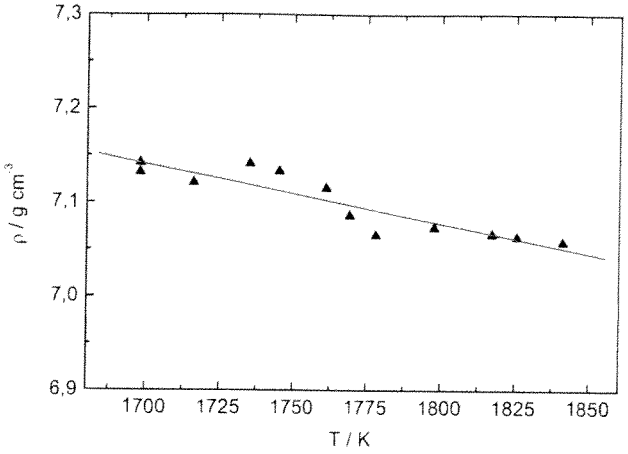

Figure 14. Density of Fe-Cr-Mo alloy in the liquid phase as function of temperature.

Density in the liquid phase. The density in the liquid phase obtained from optical dilatometry in ground-based electromagnetic levitation is shown in **Figure 14**. In the temperature range between T_{liq} −60 +80 K the density exhibits a linear temperature dependence which is given by:

$$\rho(T) = 7.10 - 6.10 * 10^{-4}\,(T - 1757\,K)\ g\,cm^{-3} \qquad (14)$$

The uncertainty of the density is < 0.04. The density in the solid phase at RT was obtained by the Archimedian method as $\rho\,(RT) = 7.85\ g\,cm^{-3}$.

Surface tension and viscosity. In **Figure 15**, surface tension as a function of temperature obtained in the ground-based sessile drop experiment is shown. The data can be well-represented by a linear fit as:

$$\sigma(T) = 1.82 - 4.05 * 10^{-4}\,(T - 1757\,K)\ Nm^{-1} \qquad (15)$$

In comparison, in **Figure 16**, the surface tension as a function of temperature obtained on a parabolic flight is shown. The data exhibit a linear temperature dependence

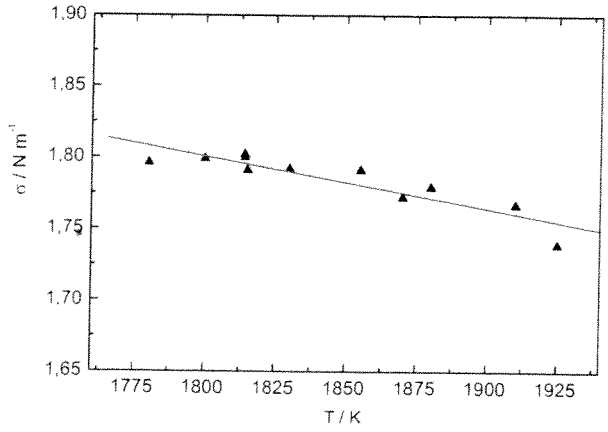

Figure 15. Surface tension of the Fe-Cr-Mo alloy as function oftemperature. Oscillating drop method in ground-based em-levitation.

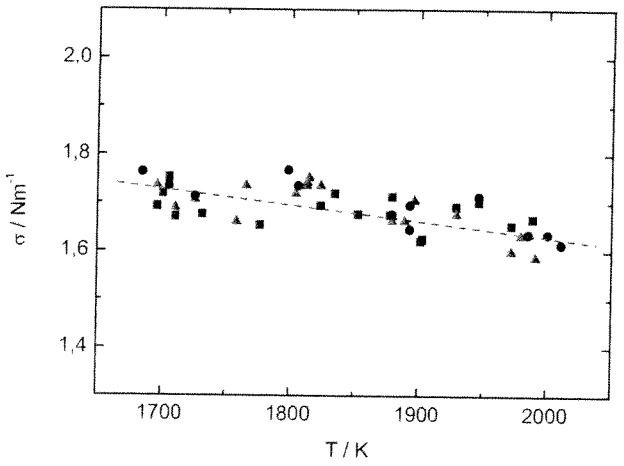

Figure 16. Surface tension of the Fe-Cr-Mo alloy as function of temperature. Oscillating drop on parabolic flight. The different symbols refer to three different parabolas.

according to:

$$\sigma(T) = 1.73 - 3.27 * 10^{-4} (T - 1757\,\mathrm{K})\,\mathrm{Nm}^{-1} \quad (16)$$

The uncertainty of the $\sigma(T_{liq})$ was obtained as ± 2 and ±4% for the ground based and parabolic flight experiments, respectively.

With the elemental surface tension values taken from the Keene [32] review, the ideal mixing surface tension is obtained as $\sigma(T_{liq}) = 1.88\ \mathrm{Nm}^{-1}$. Due to the lower surface tension of Si as compared to that of Fe, Cr, and Mo, Si can be considered as surface active element. The model of Egry [33] for an Fe-0.40at%Si alloy gives [34] $\sigma(T_{liq}) = 1.80\ \mathrm{Nm}^{-1}$ which is close to the value measured in the ground based experiment. Thus, the initial Si content of the alloy of 0.5 at% can not account for the reduced surface tension observed in the parabolic flight experiment. It is rather assumed that an increased oxygen content of the alloy processed in the parabolic flight experiment is responsible for the decreased surface tension. This demonstrates the sensitivity of the surface tension with regard to small changes in the processing conditions. The negative temperature coefficient measured in the parabolic flight experiment indicates, however, that the concentration of dissolved oxygen must have been lower than 100 ppm.

The Fe-Cr system is a weakly interacting system, and it can be described by an ideal behaviour. On the other hand, the Fe-Si system has numerous intermetallic compounds, which should also affect the structure of liquid phase so that Fe-Si can be considered as a strongly interacting system. In fact the behaviour of the surface tension of Fe-Si as a function of composition calculated by Tanaka and Lida [35] showed a pronounced non-ideal behaviour. However, in the composition range 0–10 at% Si no intermetallic compounds are present in the Fe–Si phase diagram. As such, the behaviour of the Fe-Cr-Mo, containing only 0.5 at%Si, can be considered ideal, i.e., as Fe-Cr.

In **Figure 17**, an Arrhenius plot of the viscosity obtained in the parabolic flight experiment is shown from which the prefactor, η_o, and activation energy, ΔE, were obtained as:

$$\eta_o = 0.042\,\mathrm{mPa.s}$$

$$\Delta E = 0.73\,\mathrm{eV\,atom}^{-1}$$

The viscosity at the liquidus temperature was obtained as $\eta(T) = 8.84$ mPa.s. With the oscillating cup method Sato [36] obtained a value of $\eta(T_m) = 6.35$ mPa.s for pure Fe. From more recent semi-empirical thermodynamic models [37, 38] an increase to $\eta(T_{liq}) = 8.84$ mPa.s for an alloy with ≥ 94 at% Fe is not to be expected from an alloying effect. One reason for the increased viscosity obtained on the parabolic flight, could be the formation of solid MoC precipitates. Because of the small amount of these precipitates the associated enthalpy may escape calorimetric detection. Another possibility for the large measured

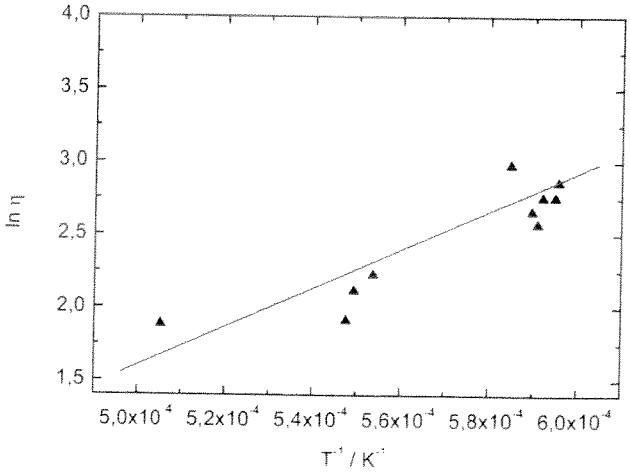

Figure 17. Viscosity of Fe-Cr-Mo alloy steel as function of inverse temperature. Oscillating drop on parabolic flight. Results from three consecutive parabolas.

Table 5. Ultrasound propagation velocities v_l and v_t for longitudinal and transversal polarization and for 2.25 MHz and 10 MHz ultrasound frequency.

	2.25 MHz	10 MHz
$v_l/10^3$ m s^{-1}	6.14 ± 0.03	6.02 ± 0.02
$v_t/10^3$ m s^{-1}	3.33 ± 0.02	3.33 ± 0.02

Table 6. Poissons's ratio and room temperature elastic constants for ultrasound frequencies of 2.25 and 10 MHz.

ν/MHz	μ	G/GPa	E/GPa	B/MPa
2.25	0.291	86.9	225	179
10	0.279	87.3	223	168

viscosity value could be an effect of dissolved oxygen. As compared to the solid phase, the solubility of oxygen in the liquid phase of pure Fe is quite large. No systematic investigation of this issue is available. The large scatter in experimental viscosities of nominally pure iron is reported in the literature [39]. The verification of these suggestions would warrant further theoretical and experimental investigation.

Velocity of sound and elastic constants. The longitudinal and transversal sound velocities at 2.25 and 10 MHz obtained from the ultrasound pulse echo measurements are listed in **Table 5**. Poisson's ratio and the elastic constants calculated from Eqs. 12 and 13a, b, c, respectively, with the density $\rho = (7.854 \pm 0.012)$ g cm^{-3}, are listed in **Table 6**. The uncertainty listed for the sound velocities was obtained from averaging the sound velocities of the three specimen of different thickness. The error in Poisson's ratio is estimated as $< 4\%$. As a conservative estimate the uncertainty in the elastic constants is $< 5\%$. The difference in the shear modulus G at $\nu = 2.25$ and 10 MHz ultrasound frequency is well within experimental uncertainty.

The sound velocities v_l and v_t, Poisson's ratio and elastic moduli fall well within the range reported in the literature [40] and trade specifications.

Summary

Thermophysical properties of an industrial Fe alloy in the solid and liquid phase relevant to casting and solidification modelling were determined in a collaborative effort by a European working group. The experimental methods applied and the results were described. Properties investigated included thermal and rheological properties. Investigations were performed in several laboratories and with different methods to obtain best-agreed-upon values. The experimental investigations were combined with phase diagram calculations and calculations of the surface tension. The methods applied included conventional techniques such as high-temperature calorimetry, dilatometry and thermal diffusivity, containerless techniques based on electromagnetic levitation such as optical dilatometry in the liquid phase in ground-based laboratory, and containerless processing under reduced gravity conditions for the measurement of the surface tension and the viscosity on board parabolic flights.

Acknowledgements

The project was supported by the European Space Agency ESA MAP programme under contract number AO-99-022. The support by the German Aerospace Center, DLR, under contract number 50WM0540, is gratefully acknowledged. Special thanks to the teams at EADS Friedrichshafen and the Microgravity User Support Center at DLR Cologne for the support in preparing and conducting the parabolic flight experiments.

References

[1] J. A. Dantzig: J. of Metals, 52 (2000), 18–21.
[2] M. Rappaz and M. Rettenmayr: Solid State and Mat. Sci. 3 (1998), 275–282.
[3] W.-S. Kim, D.-S. Kim and V. A. Kuznetsov: Int. J. Heat Mass Transf. 43 (2000) 3811–3822.
[4] R. Dippenaar: Mat. Sci. For. 654–656. (2010) 17–22.
[5] J. Etay and Y. Delannoy: Magnetohydrodynamics, 39 (2003) 445–452.
[6] K. C. Mills and J. F. Lancaster: Intl. Inst. Welding 1991, Welding Recommendations 212–796 91.
[7] K. C. Mills, B. J. Keene, G. P. Brooks and A. A. Shirley: Phil. Trans. Royal Soc. (London) A256 (1998) 911–925.
[8] N. Kubo, T. Ishii, J. Kubota and N. Aramaki: ISIJ Int (Iron Steel Inst Jpn) 42 (2002) 1251–1258.
[9] G.-G. Lee, B. G. Thomas and S.-H. Kim: Met. Mater. Int. 16 (2010) 501–506.
[10] D. M. Herlach, R. F. Cochrane, I. Egry, H.-J. Fecht and A. L. Greer: Int. Mater. Rev. 38 (1993) 273–286.
[11] I. Egry and S. Sauerland: Mat. Sci. and Eng. A178 (1994) 73–76.
[12] J. Brillo and I. Egry: Int. J. Thermophys. 24 (2004) 1155–1170.
[13] I. Egry, G. Lohöfer, I. Seyhan, S. Schneider and B. Feuerbacher: Appl. Phys. Lett. 73 (1998) 462–465.
[14] R. K. Wunderlich: High Temp. Mat. and Proc. 27 (2008) 401–412.
[15] R. K. Wunderlich and H.-J. Fecht: Mater. Trans. JIM 42 (2001) 565–573.
[16] ThermoLab project overview in High Temp. Mat. Proc. 27 (2008) 401–412.
[17] R. A. Abas, M. Hayashi and S. Seetharaman: Int. J. Thermophys. 28 (2007) 109–122.
[18] W. J. Parker, R. J. Jenkins, C. P. Butler and G. L. Abbott: J. Appl. Phys. 32 (1961) 1679–1686.
[19] Y. Takahashi, T. Azumi, and M. Sugano: Netsu-Sokutei, 8 (1981) 62.
[20] T. Nishi, H. Shibata, H. Ohta and Y. Waseda: Met. Mater. Trans. 34A (2003) 2801–2807.
[21] J. Brillo and I. Egry: Int. J. Thermophys. 24 (2003) 1155–1159.
[22] S. Krishnan, G. P. Hansen, R. H. Hauge and J. L. Margrave: High Temp. Sci. 29 (1990) 17–22.
[23] I. Egry, L. Lohöfer and G. Jacobs: Phys. Rev. Lett., 75 (1995) 4043–4046.
[24] K. Higuchi, H.-J. Fecht and R. K. Wunderlich: Adv. Engn. Mat. 9 (2007) 349–354.
[25] S. Schneider, I. Egry, R. Willnecker, R. K. Wunderlich and M. Pütz: Proc. Third Int. Symposium on Physical Sciences in Space ISPS 2007, Nara, Japan JASMA, JAXA 367 (2007).
[26] D. L. Cummings and D. A. Blackburn: J. of Fluid Mech. 224 (1991) 395–416.
[27] R. K. Wunderlich and H.-J. Fecht: Int. J. Mat. Res. form. Z. Matallkd, in print.

[28] K. Higuchi, M. Watanabe, R. Wunderlich and H.-J. Fecht: Surface Tension and Viscosity Evaluation by the Oscillating Drop Method under Droplet Rotations, Proceedings Third International Symposium on Physical Sciences in Space 2007, Nara, Japan, JASMA, JAXA 2007.
[29] T. Koseki and M. C. Flemings: Met. Trans. 28A (1997) 2385–2395.
[30] D. M. Matson: Growth Competition During Double Recalescence in Fe-Cr-Ni Alloys, in: Materials in Space - Sci., Tech., and Exploration, edited by A. F. Hepp et al., (TMS, Warrendale, PA, 1999), pp. 227–234.
[31] H. W. Kerr and W. Kurz: Int. Mat. Rev. 41 (1996) 129–164.
[32] B. J. Keene: Int. Mat. Rev. 38 (1993) 157–192.
[33] I. Egry: J. Mat. Res. 39 (2004) 6365–6366.
[34] R. K. Wunderlich, H.-J. Fecht, M. Schick, and I. Egry: Steel Res. Int., in print.
[35] T. Tanaka and L. Lida: Steel Res. 64 (1994) 21–28.
[36] Y. Sato, K. Sugisawa, D. Aoki and T. Yamamura: Meas. Sci. Technol. 16 (2005) 363–371.
[37] I. Budai, M. Z. Benko, G. Kaptay: Mater. Sci. For. 473–474. (2005) 309–403.
[38] P. Terzieff: J. Alloy and Compounds, 453 (2008) 233–240.
[39] T. Iida and R. I. L. Guthrie: The Physical Properties of Liquid Metals, Oxford: Clarendon Press, New York: Oxford University Press (1988), Chpt. 6.
[40] H. M. Ledbetter: Phys. Stat. Sol. 85 (1984) 89–96.

